A Global Climatology of Outgoing Longwave Spectral Cloud Radiative Effect and Associated Effective Cloud Properties

XIANGLEI HUANG, XIUHONG CHEN, AND GERALD L. POTTER

Department of Atmospheric, Oceanic, and Space Sciences, University of Michigan, Ann Arbor, Michigan

LAZAROS OREOPOULOS

Earth Sciences Division, NASA Goddard Space Flight Center, Greenbelt, Maryland

JASON N. S. COLE

Canadian Centre for Climate Modelling and Analysis, Environment Canada, Toronto, Ontario, Canada

DONGMIN LEE

Earth Sciences Division, NASA Goddard Space Flight Center, Greenbelt, and Goddard Earth Sciences Technology and Research, Morgan State University, Baltimore, Maryland

NORMAN G. LOEB

Radiation and Climate Branch, NASA Langley Research Center, Hampton, Virginia

(Manuscript received 24 October 2013, in final form 7 July 2014)

ABSTRACT

Longwave (LW) spectral flux and cloud radiative effect (CRE) are important for understanding the earth's radiation budget and cloud–radiation interaction. Here, the authors extend their previous algorithms to collocated Atmospheric Infrared Sounder (AIRS) and Cloud and the Earth's Radiant Energy System (CERES) observations over the entire globe and show that the algorithms yield consistently good performances for measurements over both land and ocean. As a result, the authors are able to derive spectral flux and CRE at 10-cm^{-1} intervals over the entire LW spectrum from all currently available collocated AIRS and CERES observations. Using this multiyear dataset, they delineate the climatology of spectral CRE, including the far IR, over the entire globe as well as in different climate zones. Furthermore, the authors define two quantities, IR-effective cloud-top height (CTH_{eff}) and cloud amount (CA_{eff}), based on the monthly-mean spectral (or band by band) CRE. Comparisons with cloud fields retrieved by the CERES–Moderate Resolution Imaging Spectroradiometer (MODIS) algorithm indicate that, under many circumstances, the CTH_{eff} and CA_{eff} can be related to the physical retrievals of CTH and CA and thus can enhance understandings of model deficiencies in LW radiation budgets and cloud fields. Using simulations from the GFDL global atmosphere model, version 2 (AM2); NASA's Goddard Earth Observing System, version 5 (GEOS-5); and Environment Canada's Canadian Centre for Climate Modelling and Analysis (CCCma) Fourth Generation Canadian Atmospheric General Circulation Model (CanAM4) as case studies, the authors further demonstrate the merits of the CTH_{eff} and CA_{eff} concepts in providing insights on global climate model evaluations that cannot be obtained solely from broadband LW flux and CRE comparisons.

1. Introduction

Cloud radiative feedbacks are still recognized as the greatest uncertainty in the model-based projection of future climate change (Solomon et al. 2007;

Corresponding author address: Prof. Xianglei Huang, Dept. of Atmos., Oceanic, and Space Sciences, University of Michigan, 2455 Hayward St., Ann Arbor, MI 48109.
E-mail: xianglei@umich.edu

DOI: 10.1175/JCLI-D-13-00663.1

© 2014 American Meteorological Society

Andrews et al. 2012). A diagnostic quantity closely related to the cloud radiative feedback is cloud radiative effect (CRE) at the top of atmosphere (TOA) (e.g., Cess et al. 1989; Soden et al. 2008), which is defined as the difference between TOA flux in the absence of clouds (i.e., clear-sky flux) and all-sky TOA flux. Biases in longwave (LW) TOA CRE simulated by GCMs are primarily caused by biases in simulated cloud amount, cloud-top height (CTH) [or, equivalently, cloud-top temperature (CTT)], and cloud opacity.

Model–observation comparisons of these cloud macroscopic parameters are further complicated by different retrieval techniques tailored for different satellite measurements and the ways in which monthly-mean statistics are computed for each satellite data product (e.g., Pincus et al. 2012). For example, the Moderate Resolution Imaging Spectroradiometer (MODIS) cloud algorithms use the 11-μm brightness temperature to retrieve CTH and cloud amount for low clouds and the 15-μm CO_2-slicing technique for middle and high clouds (Menzel et al. 2008). The International Satellite Cloud Climatology Project (ISCCP) retrieves CTH only from the 11-μm brightness temperature (Rossow and Schiffer 1991). The Scanning Imaging Absorption Spectrometer for Atmospheric Cartography (SCIAMACHY), on the other hand, derives CTH and cloud amount from oxygen A-band measurements by fitting the measured oxygen A-band reflectance spectrum with a modeled one, assuming a single layer of homogeneous liquid clouds (Kokhanovsky et al. 2011). The global- and annual-mean CTH from ISCCP measurement is ~4.5 km, while it is ~7.3 km from the SCIAMACHY retrievals (Koelemeijer et al. 2002; Kokhanovsky et al. 2011). For low-level clouds in the presence of a boundary layer temperature inversion, MODIS and ISCCP tend to overestimate the CTH by 2 km or more compared to the CTH retrieved from a geometric retrieval technique used by Multiangle Imaging SpectroRadiometer (MISR) observations (Garay et al. 2008; Harshvardhan et al. 2009). To make a fair comparison between models and satellite observations, significant efforts have been made to develop satellite simulators in the Cloud Feedback Model Intercomparison Project (CFMIP) Observation Simulator Package (COSP; Bodas-Salcedo et al. 2011) that can derive the CTH, among other cloud variables, from the GCM simulations in a manner that resembles as much as possible particular satellite retrievals, such as the ISCCP (Klein and Jakob 1999; Webb et al. 2001) and MODIS simulators (Pincus et al. 2012). These efforts have provided more objective ways to compare model results with observations and hence to diagnose cloud biases in global climate models. Even so, understanding the model–data discrepancies in such simulator-produced cloud fields is still not a trivial task. As clearly illustrated by Pincus et al. (2012), a good understanding of satellite data and cloud retrieval algorithms is still crucial to such simulator-based evaluations of GCM simulations.

One aim in model evaluation is to better understand and connect discrepancies in the simulated cloud field and in the simulated TOA radiation budget. Huang et al. (2010, 2013) showed that a connection can be made through the LW band-by-band CRE (i.e., the CRE over each individual absorption band used in the model's radiation scheme). These studies established algorithms to derive spectral flux (hence, spectral CRE) at 10-cm^{-1} resolution over the entire LW spectrum from collocated Atmospheric Infrared Sounder (AIRS) and Cloud and the Earth's Radiant Energy System (CERES) observations over the tropical oceans and demonstrated how such spectral CRE can be used to evaluate simulations from three GCMs. Huang et al. (2013) showed that the CRE discrepancies in a particular band among GCMs and observations can be as large as those in the LW broadband. They also revealed and quantified compensating biases in broadband LW CRE that originate from different bands. While the LW broadband CRE is affected by both cloud amount (CA) and cloud-top height, the fractional contribution of each spectral band to the LW broadband CRE (f_{CRE}) is sensitive to the cloud-top height and largely insensitive to cloud amount (Huang et al. 2010, 2013). This is because the cloud amount is a common factor on both the numerator and denominator of the ratio defined as f_{CRE}, as illustrated in Huang et al. (2010). Thus, a joint examination of f_{CRE} and LW broadband CRE offers a chance to untangle bias contributions from the CTH and CA.

Huang et al. (2010) also defined an IR-effective CTH, which can be derived by fitting the f_{CRE} of each individual absorption band and is equal to the physical CTH for a single layer of optically thick cloud in the atmosphere. Consequently, an IR-effective cloud amount can be defined as the ratio of observed LW broadband CRE to the LW broadband CRE of an overcast sky with a single-layer opaque cloud of the same CTH. The IR-effective CTH and CA defined in this way are radiation-based quantities and are thus linked directly to the TOA radiation budget. We can then investigate how such IR-effective cloud properties agree with cloud properties derived from sophisticated physical retrievals of cloud properties using satellite observations, which is another motivation behind this study.

While the studies mentioned above focus on tropical oceans, the same methodology can, in principle, be extended to obtain spectral CRE over the entire globe. A recent study by Chen et al. (2013) extended the original algorithms for computing clear-sky spectral flux

(Huang et al. 2008) to observations over land. It is therefore expected that the algorithms for cloudy-sky observations can be extended to the entire globe as well, and this is precisely one of the objectives of this study. With AIRS having collected more than 10 yr of data by the end of 2012, it is pertinent to derive LW spectral flux and CRE over the entire globe from a full decade of such collocated AIRS and CERES observations, to document their climatology, and to explore how they can be used in GCM evaluations, especially connecting evaluations of simulated macroscopic cloud fields and TOA LW radiation budgets. This study is then an extension of the previous studies that establish the algorithm for deriving spectral flux and CRE from collocated AIRS and CERES measurements and demonstrate the merit of such spectral quantities in GCM evaluation. This study is aimed at depicting the global climatology of LW spectral CRE for the first time, interpreting such climatology with IR-effective cloud properties, and exploring the usage of such IR-effective properties in GCM evaluation. The remaining sections are organized as follows. The extended algorithm for global band-by-band LW flux CRE observations and its validation are described in section 2. Section 3 showcases the global climatology of spectral flux and CRE and delineates contributions of the far IR (0–600 cm^{-1}) to the zonal-mean TOA LW radiation budget. Section 4 defines the IR-effective CTH and CA, compares them with their physically retrieved counterparts, and explores their use in GCM evaluations. Conclusions and further discussions are provided in section 5.

2. Data, algorithms, and validation

Observational data and forward modeling tools used in this study are described in section 2a. The algorithms are summarized in section 2b. Section 2c presents the validations: that is, the comparisons with collocated CERES data.

a. Data and forward models

Following the approach in Huang et al. (2008, 2010), collocated *Aqua* AIRS and CERES observations are used in this study. AIRS is a grating spectrometer measuring spectral radiances in 2378 channels in the thermal IR and near IR (Aumann et al. 2003; Chahine et al. 2006). CERES has two broadband radiometers that enable estimates of the TOA broadband outgoing radiant flux for both longwave and shortwave. Relevant details on both instruments and observation collocation procedures can be found in Huang et al. (2008). For this study, we use level 1B (L1B) calibrated radiances from AIRS, version 5, and the latest version of the CERES Single Satellite Footprint (SSF) data product, edition 3 (Loeb et al. 2012).

As in Chen et al. (2013), the Moderate Transmission Code, version 5 (MODTRAN5; Anderson et al. 2007) is used as the forward radiative transfer model to build the algorithms. The surface spectral emissivity in the forward modeling is based on the Advanced Spaceborne Thermal Emission Reflection Radiometer (ASTER) Spectral Library, version 2.0 (Wilber et al. 1999; Baldridge et al. 2009). More details about MODTRAN5 and the ASTER Spectral Library can be found in Chen et al. (2013).

To compare with CTH and CA from the physical retrievals of satellite observations, we use the cloud properties produced by the CERES–MODIS retrieval algorithms described in Minnis et al. (2011a) and Minnis et al. (2011b). The CERES–MODIS data were obtained from the Global Energy and Water Exchange Project (GEWEX) Cloud Assessment database (Stubenrauch et al. 2013). Following the convention in the GEWEX database, we denote the CERES–MODIS dataset as MODIS–CE. Given the data availability, the comparisons related to MODIS–CE retrievals will be made for the period 2003–09.

b. Algorithms extended to global observations

1) CLOUDY-SKY OBSERVATIONS OVER SNOW- AND ICE-FREE LAND

Huang et al. (2008, 2010) developed spectral anisotropic distribution models (ADMs) for all CERES subscene types over the tropical oceans (note, the subscene type is called "discrete interval" in Loeb et al. 2005). Using such spectral ADMs and scene-type information from the collocated CERES SSF dataset, spectral flux over each AIRS channel can be derived. Spectral fluxes over frequencies not covered by the AIRS instrument are then computed using a multivariate linear prediction scheme based on principal component decompositions, which is prebuilt for each subscene type (please refer to Huang et al. 2008 for details about this scheme). With these two steps, spectral fluxes at a 10 cm^{-1} interval over the entire longwave spectrum can be derived, and spectral CRE can be computed the same way as the CERES broadband CRE. Chen et al. (2013) extended the original clear-sky algorithms to all clear-sky scene types over land by taking into account the different types of land surface spectral emissivity.

In principle, the same extension method of Chen et al. (2013) can be applied to the cloudy-sky algorithms. However, the definitions of subscene types in the CERES cloudy-sky ADM are more complex than those of the CERES clear-sky ADM. The number of subscene types used in Huang et al. (2010) for cloudy-sky ADMs is two orders of magnitude greater than the number used in

Huang et al. (2008) for clear-sky ADMs. Therefore, if we were to simply repeat what Chen et al. (2013) did, computationally it would be extremely demanding to build a full set of cloudy-sky spectral ADMs. However, unlike the clear-sky case, where surface spectral emissivity always affects the outgoing longwave radiation (OLR), some cloudy-sky cases have zero sensitivity to the surface spectral emissivity. For example, if the cloud is overcast and optically thick, then no photon of any frequency originating from the surface can reach the TOA, which means that the spectral ADM built by Huang et al. (2010) for this cloudy scene type can simply be used over land without any modification. With this in mind, we developed a semiempirical correction to the spectral ADMs developed by Huang et al. (2010). The correction takes the land surface spectral emissivity into account and makes it useable for cloudy-sky measurements over land, thus bypassing the need to compute spectral ADMs using the more exact but time-consuming methods for all subscene types. The details of this correction method are described in appendix A.

The OLR derived using this correction method for AIRS cloudy-sky measurements (OLR_{AIRS_Huang}) over land is compared with the collocated CERES OLR (OLR_{CERES}). Following the convention in the CERES SSF dataset, the comparison is performed for desert and nondesert land areas separately. Table 1 summarizes the comparison results for each combination of CA and surface–cloud temperature difference (ΔT_{sc}) used in the definition of subscene types. For each combination of CA and ΔT_{sc}, the mean OLR difference is generally within 1%: that is, within the 2-sigma radiometric uncertainty of CERES measurements (Loeb et al. 2007), which translates to a ~(2.0–2.5) $W\,m^{-2}$ uncertainty in the all-sky OLR. The difference is generally larger for the middle-cloud cases ($15\,K < \Delta T_{sc} < 40\,K$) than for other cloudy cases. These results are largely consistent with the comparisons in Huang et al. (2010) for cloudy-sky observations over tropical oceans, indicating that the performance of this method is consistent across both ocean and land. Figure 4c in Huang et al. (2010) shows that cloud spatial heterogeneity can affect the difference $OLR_{Huang_AIRS} - OLR_{CERES}$, which should be also responsible for the large standard deviations shown in some grids in Table 1. For discussion of other possible sources of errors in $OLR_{Huang_AIRS} - OLR_{CERES}$, please refer to Huang et al. (2010) for more information.

2) ALL-SKY OBSERVATIONS OVER SNOW AND ICE SURFACES

We explicitly build spectral ADMs for each subscene type of snow and ice surfaces defined in Table 5 of Loeb et al. (2005). In this case, such an approach is

TABLE 1. Differences between cloudy-sky OLR estimated from AIRS spectra and the collocated cloudy-sky CERES OLR for different combinations of CA and ΔT_{sc}. Nondesert lands and deserts are considered separately. Data for the entire year of 2004 are used. Mean ± one standard deviation of the differences is given for each combination. The fractional mean difference, i.e., $(OLR_{AIRS_Huang} - OLR_{CERES})/OLR_{CERES}$, is shown in parentheses.

	Deserts			Nondesert lands		
ΔT_{sc} CA	<15 K	15–40 K	>40 K	<15 K	15–40 K	>40 K
0.001–0.5	2.44 ± 3.79 (0.9%)	3.25 ± 5.12 (1.2%)	1.49 ± 7.61 (0.5%)	2.34 ± 2.86 (0.8%)	3.62 ± 4.48 (1.3%)	2.84 ± 5.94 (1.0%)
0.5–0.75	2.79 ± 4.16 (1.1%)	3.34 ± 7.80 (1.3%)	1.39 ± 12.75 (0.5%)	2.90 ± 3.86 (1.1%)	4.24 ± 7.25 (1.7%)	2.61 ± 11.38 (1.0%)
0.75–0.999	2.67 ± 3.67 (1.1%)	1.45 ± 6.47 (0.6%)	−1.17 ± 10.97 (−0.5%)	2.81 ± 3.56 (1.2%)	3.14 ± 6.68 (1.4%)	0.47 ± 11.45 (0.2%)
0.999–1.0	2.61 ± 2.80 (1.2%)	3.15 ± 4.00 (1.6%)	1.28 ± 6.64 (0.7%)	2.86 ± 2.83 (1.3%)	4.04 ± 4.33 (2.0%)	2.48 ± 7.16 (1.5%)

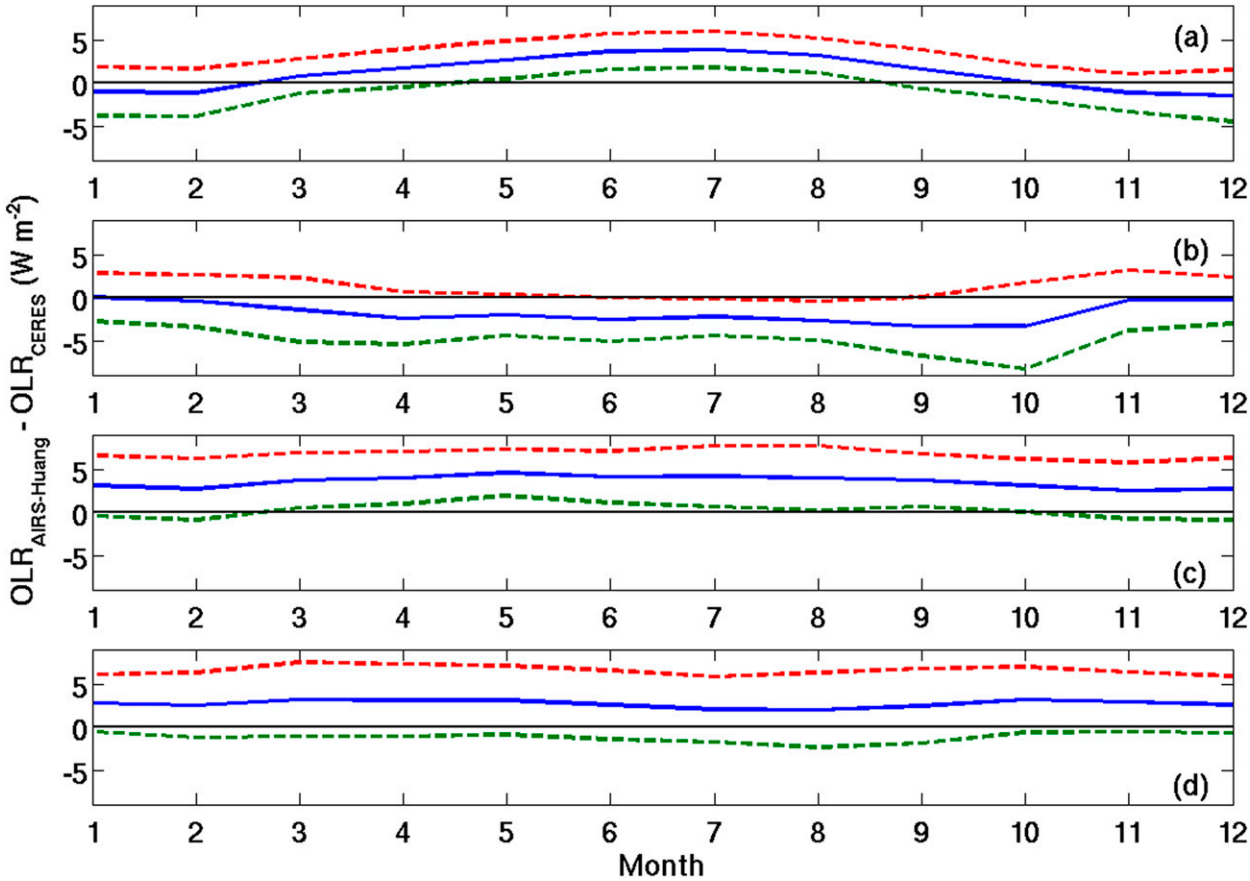

FIG. 1. (a) Blue solid line denotes the monthly-mean $OLR_{AIRS_huang} - OLR_{CERES}$ difference for all collocated clear-sky daytime observations over snow and ice surfaces in 2004. Red and green dotted lines denote the $\pm 1\sigma$ from the mean, respectively. (b) As in (a), but for clear-sky nighttime observations. (c) As in (a), but for cloudy-sky daytime observations. (d) As in (a), but for cloudy-sky nighttime observations.

computationally affordable because the atmosphere above snow and ice surfaces is usually dry and cold and the lower troposphere is often nearly isothermal. As a result, many fewer subscene types are needed, compared to other land surface types (Loeb et al. 2005). Total precipitable water and lapse rate are not used in the definition of clear-sky subscene types over the snow and ice surfaces while for surface temperatures (T_s) and surface–cloud temperature difference (ΔT_{sc}), only two intervals are used. The clear-sky fraction (f_{clr}) is divided into six bins (0–0.001, 0.001–0.25, 0.2–0.5, 0.5–0.75, 0.75–0.99, and 1.0). To better account for seasonal variation and improve performance, the spectral ADMs over the snow and ice surfaces are built separately for each season. This approach accommodates the seasonal cycle of surface temperature and other associated properties in the cryosphere better than a single set of spectral ADMs for all seasons.

Figure 1 shows the monthly statistics of $OLR_{AIRS_Huang} - OLR_{CERES}$ over all the snow and sea ice surfaces for each month in 2004. The annual clear-sky OLR difference is 1.1 W m^{-2} for the daytime observations and -1.8 W m^{-2} for the nighttime observations. For cloudy-sky OLR, the daytime-mean difference is 3.5 W m^{-2} and that for nighttime is 2.7 W m^{-2}. The standard deviation of $OLR_{AIRS_Huang} - OLR_{CERES}$ is ~3 W m^{-2} for clear-sky and ~4 W m^{-2} for cloudy-sky results; both values are comparable to their counterparts for oceans and nonfrozen land surfaces.

c. *Multiyear comparisons with collocated CERES OLR*

The algorithms described above, along with those by Huang et al. (2008, 2010) and Chen et al. (2013), make it possible to derive spectral fluxes from collocated AIRS and CERES observations over the entire globe. Figure 2 shows the annual statistics of $OLR_{AIRS_Huang} - OLR_{CERES}$ for the period of 2003–11. The clear-sky annual-mean difference is between -0.67 and -0.38 W m^{-2} for the nighttime and between -0.34 and 0.42 W m^{-2} for the

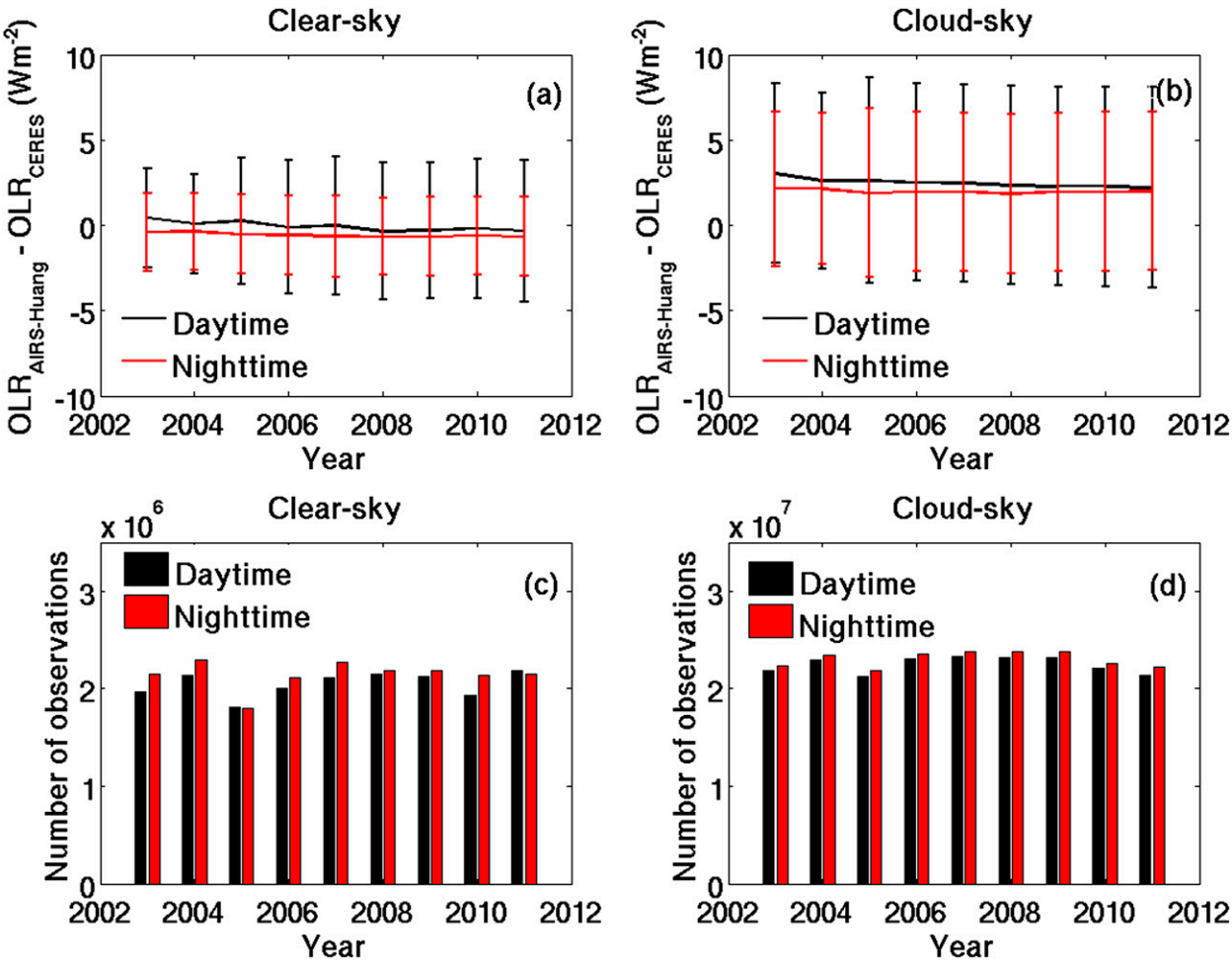

FIG. 2. (a) Annual means of clear-sky $OLR_{AIRS_Huang} - OLR_{CERES}$ differences over the entire globe for 2003–11. The vertical lines with ticks denote the $\pm 1\sigma$ from the mean. Daytime and nighttime results are plotted separately. (b) As in (a), but for cloudy-sky observations. (c) Number of collocated AIRS and CERES clear-sky observations in each year from 2003 to 2011. Daytime and nighttime results are shown separately. (d) As in (c), but for cloudy-sky observations.

daytime. The range of cloudy-sky annual-mean difference is 1.85–2.12 $W\,m^{-2}$ for the nighttime and 2.20–3.0 $W\,m^{-2}$ for the daytime. These statistics are consistent with the statistics published before for the tropical oceans and for clear sky over lands (Huang et al. 2008, 2010; Chen et al. 2013). Though the mean difference of $OLR_{AIRS_Huang} - OLR_{CERES}$ is systematically positive for cloudy-sky cases, the fractional difference is only ~0.93%. For the nine years examined here, the standard errors of annual-mean differences are 0.06 $W\,m^{-2}$ and 0.05 $W\,m^{-2}$ for clear sky and cloudy sky, respectively. The numbers of collocated clear-sky observations and cloudy-sky observations are largely consistent from year to year (Figs. 2c,d).

We also calculate the spectral CRE in the same way as the broadband CRE is computed from the CERES all-sky and clear-sky fluxes. Figures 3a and 3b show the December–February (DJF) and June–August (JJA) zonal-mean broadband LW CRE anomalies at different latitudes, obtained by integrating the spectral CRE anomalies in all frequencies. The anomaly is defined as the deviation from the corresponding climatology derived from the entire dataset (i.e., 2003–11). The counterparts from the CERES SSF dataset are shown in Figs. 3c and 3d, respectively. Our results are consistent with the CERES results in both the magnitude and time evolution of the anomalies, and have a correlation coefficient greater than 0.96 for both comparisons.

Figure 4 shows the multiyear (2003–11) global-mean spectral CRE in 10 cm^{-1} spectral intervals and the mean spectral CRE over four different climate zones, as derived from the collocated AIRS and CERES observations. For all climate zones, the spectral CRE in the center of the CO_2 band is zero, as expected given zero

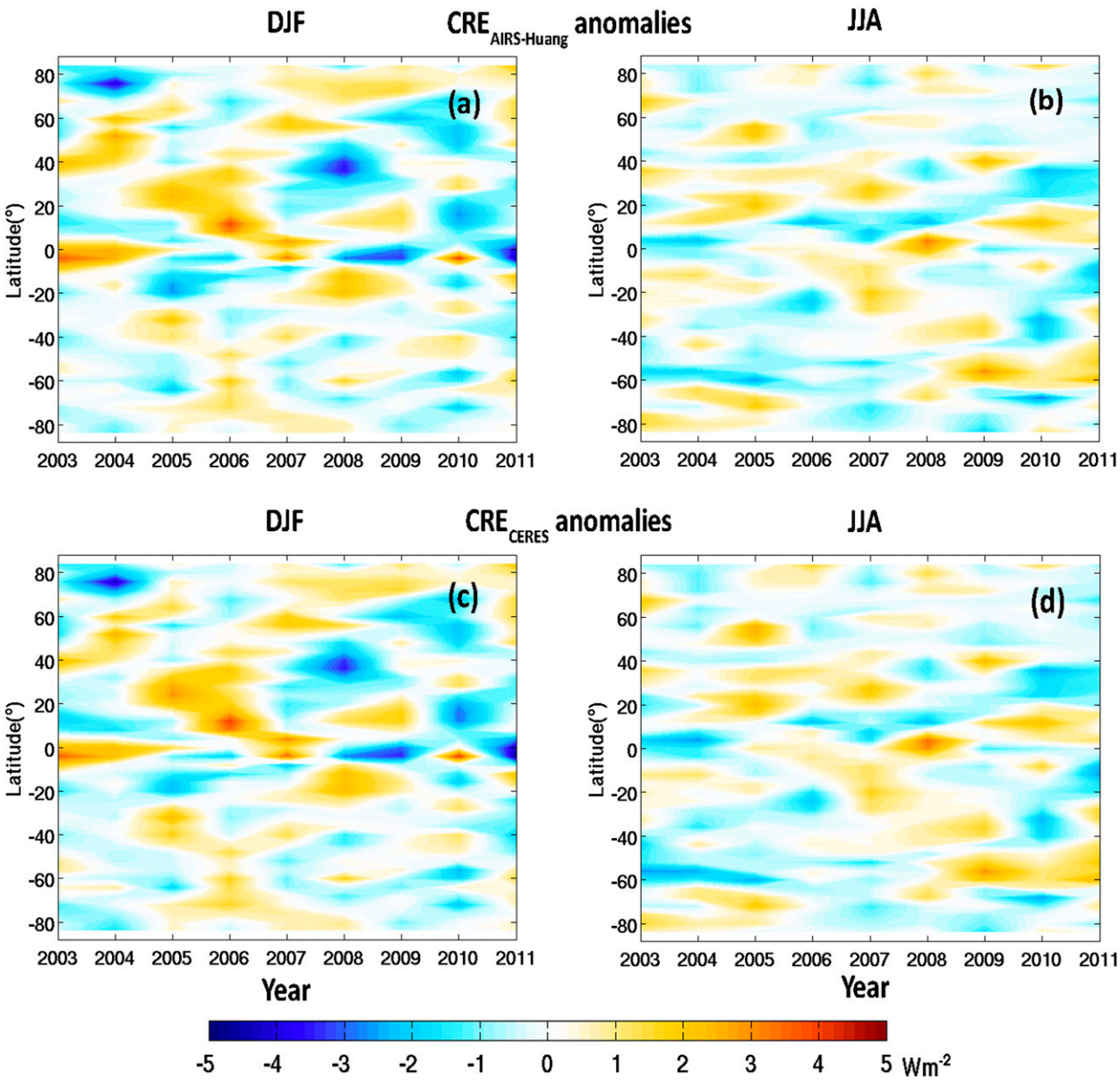

FIG. 3. (a) DJF zonal-mean LW broadband CRE anomalies (i.e., deviations from climatological means) derived from AIRS observations collocated with CERES measurements. (b) As in (a), but for JJA. (c),(d) As in (a),(b), but derived directly from the CERES SSF datasets. A latitude bin of 4° is used. The correlation between (a) and (c) is 0.97, and the correlation between (b) and (d) is 0.96.

radiative contribution of tropospheric clouds to the TOA spectral flux in this spectral region.

All comparisons above indicate that the algorithms for deriving spectral flux from global collocated AIRS and CERES measurements perform well for all the years that we have processed. This strengthens our confidence in using the derived multiyear spectral flux dataset for relevant climate studies and model evaluations. For this purpose, we average the spectral CREs from collocated AIRS and CERES observations for each month between January 2003 and December 2011 onto 2° × 2.5° grid boxes to form monthly-mean gridded data. This dataset is then used for further study in the following sections.

3. Global climatology of LW TOA spectral CREs

a. Climatology and contrast between the mid-IR and the far IR in different climate zones

Figure 4 shows the multiyear means of spectral CRE at 10 cm^{-1} intervals over different latitudinal zones: namely, the deep tropics (5°S–5°N), the extended tropics (30°S–30°N), the Southern Hemisphere extratropics (30°–90°S),

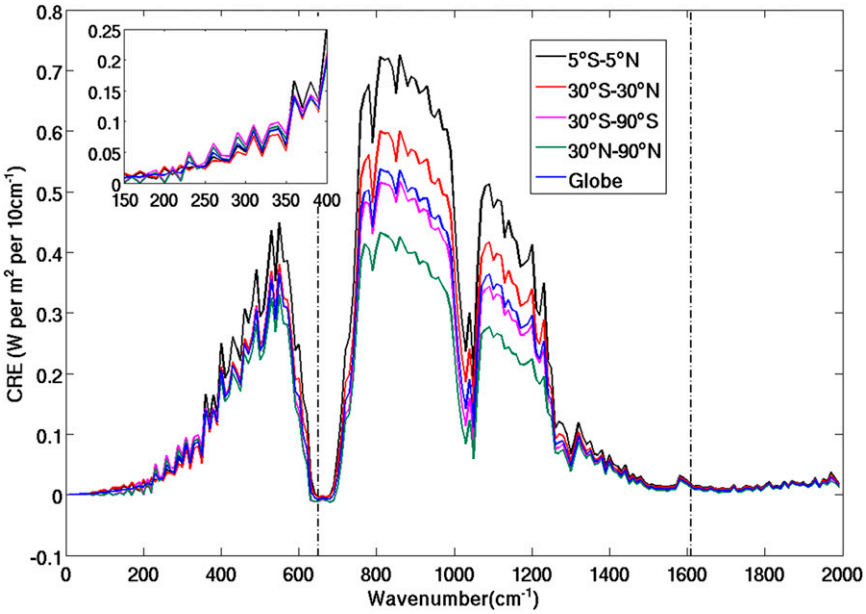

FIG. 4. Multiyear (2003–11) averages of spectral CRE at 10 cm^{-1} intervals over climate zones provided in the legend. The inset zooms in the 150–400 cm^{-1} spectral region. The vertical dashed–dotted lines denote the start and end frequencies of the AIRS thermal IR detectors.

the Northern Hemisphere extratropics (30°–90°N), and over the entire globe. The spectral CREs in the window and ozone bands vary considerably from one climate zone to another, but the amplitudes of the spectral CREs follow the same tendency as the amplitudes of the broadband LW CREs. For example, the broadband LW CRE over the deep tropics is 37.9 $W m^{-2}$ and is the largest among all climate zones shown in Fig. 4. The broadband LW CRE over the 30°–90°S zone, 27.15 $W m^{-2}$, is the second smallest and is only larger than that of the 30°–90°N zone. The same order is preserved for the amplitude of spectral CREs in the window and ozone bands, as can be seen by the ordering of the curves in Fig. 4.

However, in the far IR, such correlation with the LW broadband CRE holds only for frequencies $> \sim 350\,cm^{-1}$. As shown in the insert in Fig. 4, the sequence of color lines has changed for frequencies lower than 350 cm^{-1}. For most of the 200–350 cm^{-1} spectral region, the largest spectral CRE is that of the extratropics of the Southern Hemisphere and the second largest is that of its Northern Hemisphere counterpart. Such contrast between far IR and mid-IR for the amplitudes of spectral CREs over different regions is consistent with Wien's displacement law: as the temperature decreases, more emission originates from the far IR rather than from the mid-IR.

Figure 5 shows two cases of spectral CREs using standard sounding profiles at different climate zones (McClatchey et al. 1972) and two different ice cloud-top heights, one at 6 km (Fig. 5a) and another at 10 km (Fig. 5b). Similar to Fig. 4, Fig. 5 shows that, while the spectral CRE of the subpolar winter is the smallest in the window band and ozone band, it is the largest in all frequencies $< \sim 500\,cm^{-1}$ (i.e., the bulk of the far IR). This applies to cloud-top heights in both cases examined here. Note that, because the far IR is not covered by the AIRS instrument, the far-IR results in Fig. 4 are derived using multilinear regression schemes based on principal component decomposition techniques, as explained earlier. Nevertheless, the contrast between far IR and mid-IR in Fig. 4 is consistent with our understanding of spectral CRE and underscores the need of monitoring far-IR spectral regions from space, as discussed further in the next subsection.

b. *Contributions of the far IR to the TOA LW broadband radiation*

It has been known for decades that the far IR plays an important role in the earth radiation budget (see, for example, the review by Harries et al. 2008 and references therein). Although the far IR has been observed from the surface (e.g., Turner and Mlawer 2010), decades have passed since the last direct far-IR spectral observations of Earth from space that took place between April 1970 and January 1971, when the infrared interferometer spectrometer (IRIS-D; Hanel et al. 1972) measured the 400–600 cm^{-1} portion of the far IR. Therefore, it is instructive to use our derived spectral flux and CRE to examine contributions of the far IR to the TOA LW broadband radiation budget, especially

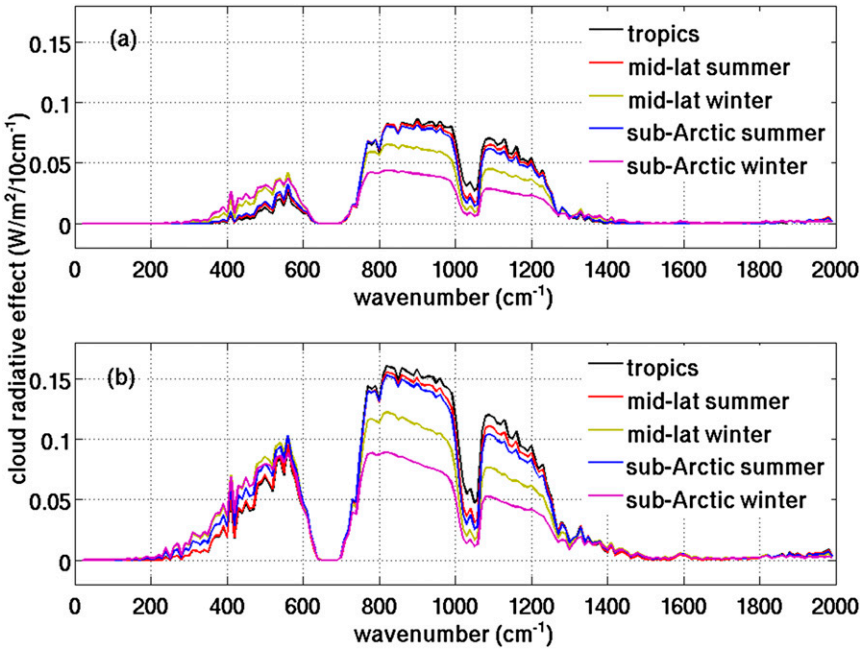

FIG. 5. (a) The spectral CRE at 10 cm^{-1} intervals for a one-layer opaque cloud with its top at 6 km. Standard sounding profiles in different climate zones (McClatchey et al. 1972) are used in the calculation and shown in the legends. (b) As in (a), but with a cloud-top height at 10 km.

as a function of latitude. Figure 6 shows such contributions for the clear-sky OLR, all-sky OLR, and LW CRE based on results from 2003 to 2011. For both clear-sky and all-sky broadband OLR, the far IR contributes more in the polar regions than in the other climate zones. The far-IR contribution to clear-sky OLR monotonically decreases from ~(0.55–0.65) in the polar regions to ~0.43 in the deep tropics. The far-IR contribution to all-sky OLR follows a similar trend but for a local maximum in the tropics at ~7°N, which is the climatological position of ITCZ and thus can be explained by the presence of deep convective clouds. As for the LW broadband CRE, the far-IR contribution is smallest in the tropics [~(0.20–0.25)] and largest in the polar regions (0.45–0.55). The far-IR contribution to the LW CRE is largely determined by the nature of clear-sky radiation. For the tropics, the mid-IR window band dominates the clear-sky OLR, while the far-IR portion of the clear-sky OLR originates from the middle and upper troposphere. As a result, clouds in the upper and middle troposphere are effective in blocking the mid-IR radiation but not as effective in the far IR, because a large portion of the far-IR flux reaching the TOA originates from levels above the clouds. For the polar regions, temperatures are much colder than in the tropics and the atmosphere is much drier as well. As a result, the surface emission contributes significantly to the far-IR portion of clear-sky OLR, and the effective emission level of water vapor is lower in the atmosphere. Therefore, clouds are more effective in blocking the far-IR portion of OLR that would have reached the TOA under clear skies.

4. IR-effective cloud properties derived from the spectral CRE

To provide useful diagnostics for model evaluation and to link the evaluations of the LW radiation budget with that of cloud macroscopic properties, in this section we further explore the concepts of IR-effective CTH and CA that were briefly discussed in section 4 of Huang et al. (2010).

a. *Definition of the IR-effective* CTH *and* CA

For a set of given spectral CRE (or band-by-band CRE as calculated by the GCMs), it is trivial to compute the fractional contribution of a band to LW CRE [$f_{\mathrm{CRE}}(\Delta\upsilon)$], and we denote this as $f_{\mathrm{CRE_data}}(\Delta\upsilon)$, where $\Delta\upsilon$ is the spectral interval or bandwidth. Then with appropriate temperature and humidity profiles, we can assume a one-layer optically thick cloud at different altitude z and compute the corresponding f_{CRE}, denoted as $f_{\mathrm{CRE_1CLD}}(\Delta\upsilon; z)$. We then define a cost function

$$\mathrm{err}(z) = \sum_{i=1}^{N} [f_{\mathrm{CRE_data}}(\Delta\upsilon_i) - f_{\mathrm{CRE_1CLD}}(\Delta\upsilon_i; z)]^2, \quad (1)$$

where the subscript i denotes the ith spectral interval or band. The IR-effective cloud-top height ($\mathrm{CTH_{eff}}$) is

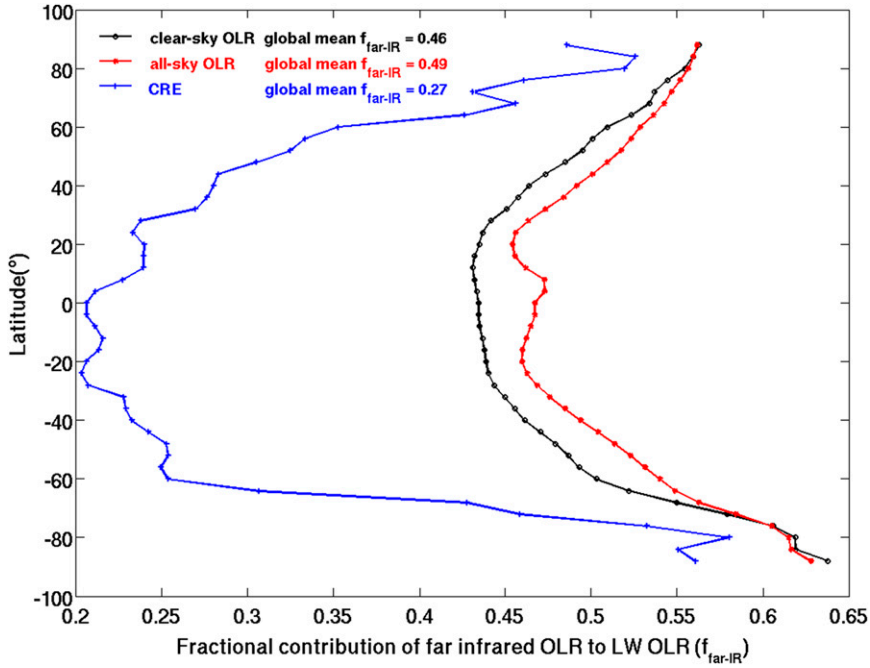

FIG. 6. Latitudinal contribution of the far IR (0–600 cm^{-1}) to the clear-sky OLR (black line), the all-sky OLR (red line), and the LW broadband CRE (blue line) based on multiyear averaged spectral flux and CRE derived from collocated AIRS and CERES observations. The global-mean contributions of the far IR are also shown using the corresponding colors.

defined as the altitude for which err(z) attains its minimum, which can be obtained by either brute-force calculation or a bisection method by varying z in an offline radiative transfer model, such as MODTRAN5. With the CTH_{eff} and the same temperature and humidity profiles used in (1), we can compute the LW broadband CRE for an overcast sky with cloud top at CTH_{eff}, denoted as $CRE_{overcast_1CLD}(LW; CTH_{eff})$. Then the effective cloud amount (CA_{eff}) can be defined as

$$CA_{eff} = CRE(LW)/CRE_{overcast_1CLD}(LW; CTH_{eff}), \quad (2)$$

where CRE(LW) is either the observed or GCM-simulated LW broadband CRE.

Simply put, CTH_{eff} and CA_{eff} are the stepwise best fit of a one-layer opaque cloud model to the actual spectral (or band-by-band) CRE data, which might be obtained from observations, from GCM simulations, or from reanalysis. CTH_{eff} and CA_{eff} are derived from LW spectral CRE alone. Thus, strictly speaking, they are radiative quantities, and their diagnostics can be directly linked to broadband CRE and the radiation budget. At the same time, if they can be related to cloud physical macroscopic properties as well, they will enable connections between diagnostics of radiation budget and cloud simulations. Moreover, if CTH_{eff} and CA_{eff} diagnosed from monthly-mean output are meaningful, diagnostics of this kind can be then potentially applied to a wide range of model outputs, such as those archived by phase 3 and phase 5 of the Coupled Model Intercomparison Project (CMIP3 and CMIP5).

In practice, we find that, for given temperature and humidity profiles, the fitted CTH_{eff} changes little when spectral bandwidth varies from 10 cm^{-1} to the typical bandwidths of GCM radiation schemes. We also find that estimations of CTH_{eff} and CA_{eff} from monthly-mean data are more sensitive to the humidity than the temperature profiles when the water vapor far-IR band is included in the fitting. This is because 1) the contribution of upper-tropospheric humidity to the far-IR band flux is significant as long as the cloud top is below the upper troposphere; and 2) upper-tropospheric humidity can exhibit large variation within a month, especially in regions where wet and dry regimes alternate. Since we are aiming at having diagnostics of CTH_{eff} and CA_{eff} solely from monthly averaged band-by-band CREs, we excluded the far-IR band (or the combined band in the GCM, which includes the far-IR band; Huang et al. 2013) in our fitting. For similar reasons, we exclude the ozone band in our derivation because the ozone vertical profiles can affect the fitting results, and not all GCMs analyzed have employed realistically time-varying ozone profiles in the simulation. For results described in the following subsections, CTH_{eff} and CA_{eff} are derived from fitting the

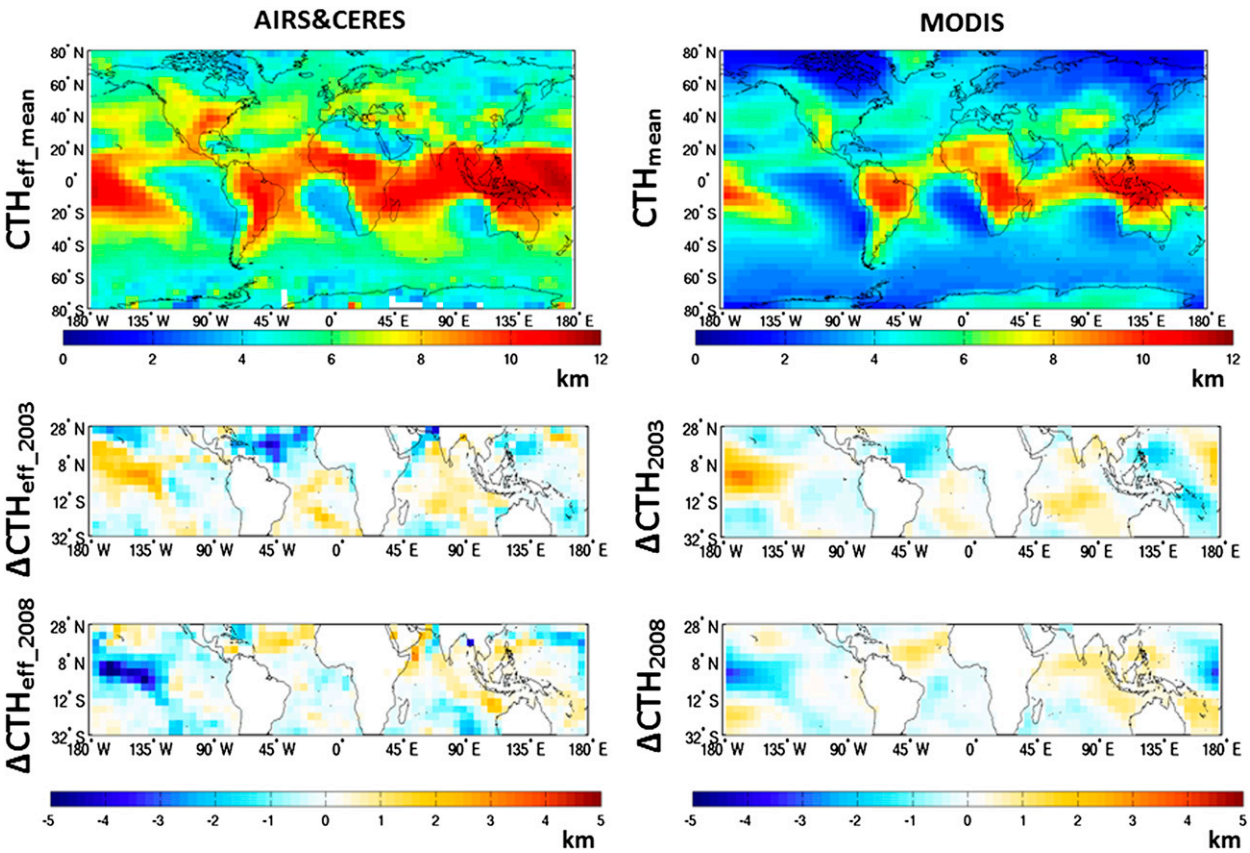

FIG. 7. (top) (left) Multiyear (2003–09) DJF mean of CTH_{eff} inverted from collocated AIRS and CERES band-by-band CREs; (right) 2003–09 DJF-mean CTH from the MODIS–CE dataset. (middle) (left) Deviation of CTH_{eff} of December 2002–February 2003 (an El Niño winter) from its multiyear mean in (top left) (denoted as ΔCTH_{eff_2003}); (right) deviation of MODIS–CE CTH of December 2002–February 2003 from its multiyear mean (denoted as ΔCTH_{2003}). (bottom) As in (middle), but for December 2007–February 2008 (a La Niña winter). All data are averaged onto 10° × 8° grid boxes. Note that ΔCTH panels use identical color scales.

band-by-band CREs of all other LW bands. As shown in Fig. 7b in Huang et al. (2010), for each band, the change of f_{CRE} with respect to cloud-top height is monotonic. Therefore, exclusion of two bands does not significantly affect the results of CTH_{eff} fitting.

b. *Comparisons of* CTH_{eff} *and* CA_{eff} *with MODIS–CE cloud retrievals*

Using the approach outlined in section 4a and the monthly-mean temperature and humidity profiles from the Interim European Centre for Medium-Range Weather Forecasts (ECMWF) Re-Analysis (ERA-Interim; Dee et al. 2011), we compute the CTH_{eff} and CA_{eff} from the monthly-mean band-by-band CRE that we derived from collocated AIRS and CERES observations and then compare them with the CTH and CA from MODIS–CE cloud retrievals (Minnis et al. 2011a,b). As noted in section 2, this comparison is for 2003–09 only. Definitions of bands are the same as those used in Huang et al. (2013).

The DJF climatology of CTH_{eff} and MODIS–CE CTH for 2003–09 (top panels in Fig. 7) largely agrees with each other over regions with frequent occurrence of tropical deep convection. For regions dominated by low clouds, the CTH_{eff} is generally higher than the MODIS–CE CTH. Such systematic positive differences between CTH_{eff} and CTH from physical retrievals in low-cloud regions are related to the limitation of our one-layer opaque cloud assumption and the temporal variability of clouds within monthly time scale, especially when multilayer clouds occur in the area of interest. In appendix B, we perform a simple numerical exercise to explain why the definition of CTH_{eff} leads to an overestimate of height for that situation compared to a monthly average of physically retrieved CTH.

The corresponding climatology of the CA_{eff} and the MODIS–CE cloud amount also agree with each other over most of the globe (top panels in Fig. 8). One distinct discrepancy in both Fig. 7 and Fig. 8 is over the Sahara Desert, where the MODIS–CE climatology shows a much higher CTH and much smaller CA than the CTH_{eff} and CA_{eff} inverted from the band-by-band CRE. A further examination of the cloud emissivity indicates that these clouds

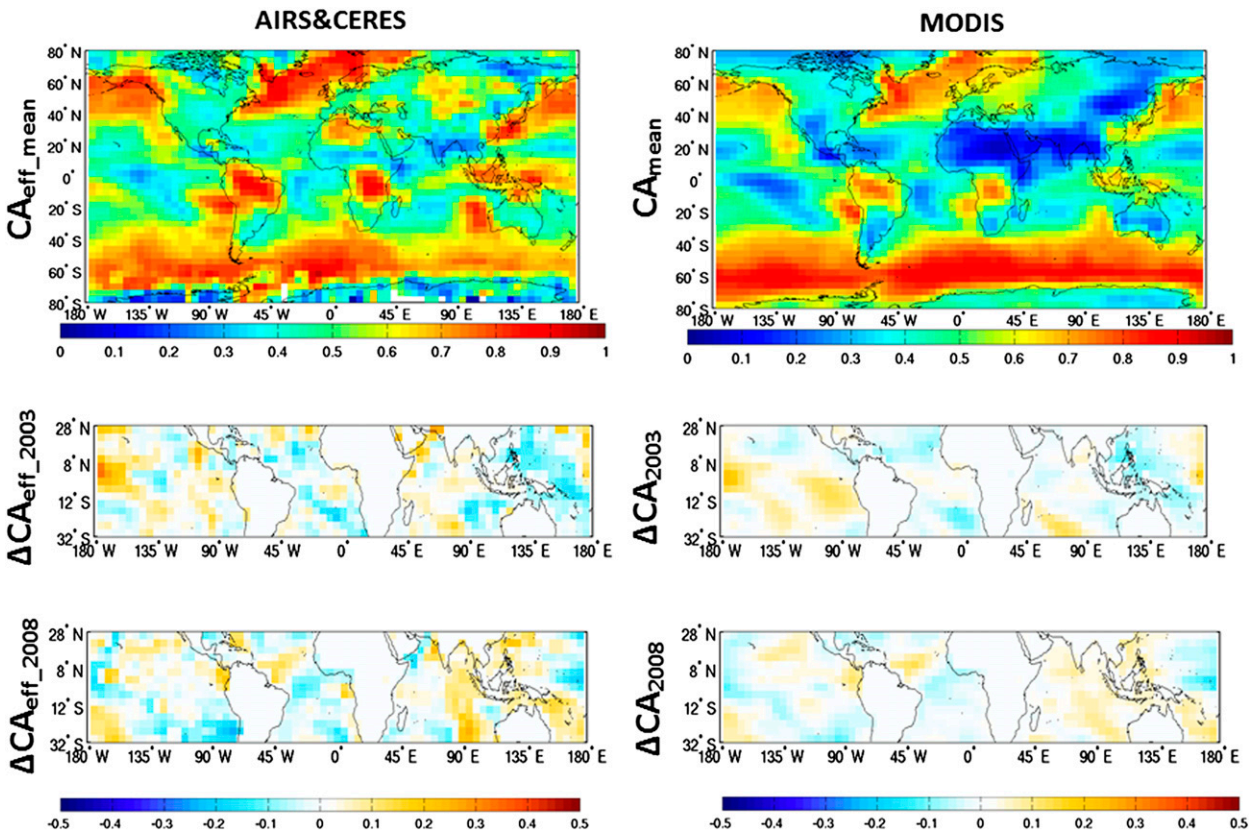

FIG. 8. As in Fig. 7, but for (left) the IR-effective cloud amount and (right) the MODIS–CE cloud amount.

over the Sahara Desert are optically thin cirrus. Such features over the Sahara are also shown in the level 3 cloud product of MODIS Collection 5.1 (King et al. 2013). Given the assumption of fully opaque clouds used in the definition of CTH_{eff}, it is not surprising that the inversion of the band-by-band CRE incorrectly interprets such features as clouds of lower altitude and larger amount.

Using an El Niño (DJF of 2003) and a La Niña (DJF 2008) winter as examples, the middle and lower panels in Figs. 7 and 8 show the interannual variations of CTH_{eff} and CA_{eff} versus those of MODIS–CE CTH and CA. As expected, the CTH and CA of the tropical central Pacific increase in the El Niño winter as a result of the shift of the ascending branch of the Pacific Walker circulation from the western to the central Pacific. Correspondingly, the CTH and CA in the tropical western Pacific decrease. Changes in the clouds over the tropical Atlantic basin via teleconnection, commonly known as the atmospheric bridge (Klein et al. 1999), can also be seen in both Fig. 7 and Fig. 8. Correspondingly, opposite changes happen during the La Niña winter for these areas. Although interannual variations of CTH_{eff} (CA_{eff}) and MODIS–CE CTH (CA) have discernible differences, as shown in Figs. 7 and 8, both CTH_{eff} and CA_{eff} can largely capture the interannual variations associated with different phases of ENSO events, and the gross features are consistent with the MODIS–CE CTH and CA changes in terms of both relative magnitude and spatial patterns. Note that CTH_{eff} and CA_{eff} inverted from monthly-mean fields are purely diagnostic variables. No one-to-one matching with physical cloud variables should be expected. Nevertheless, Figs. 7 and 8 show that the CTH_{eff} and CA_{eff} inverted from such monthly-mean fields are meaningful for both the climatology and interannual variations associated with ENSO events.

c. *Observed and simulated zonal-mean* CTH_{eff} *and* CA_{eff}

As an extension of the GCM evaluation studies in Huang et al. (2013), we compare the CTH_{eff} and CA_{eff} from the collocated AIRS and CERES observations in 2004 with those from three atmospheric GCM simulations forced by observed SST for that year. The three GCMs used here are the same as those used in Huang et al. (2013) [i.e., the Geophysical Fluid Dynamics Laboratory (GFDL) Atmospheric Model, version 2 (AM2), the National Aeronautics and Space Administration (NASA) Goddard Earth Observing System, version 5 (GEOS-5), and the Fourth Generation Canadian Atmospheric General

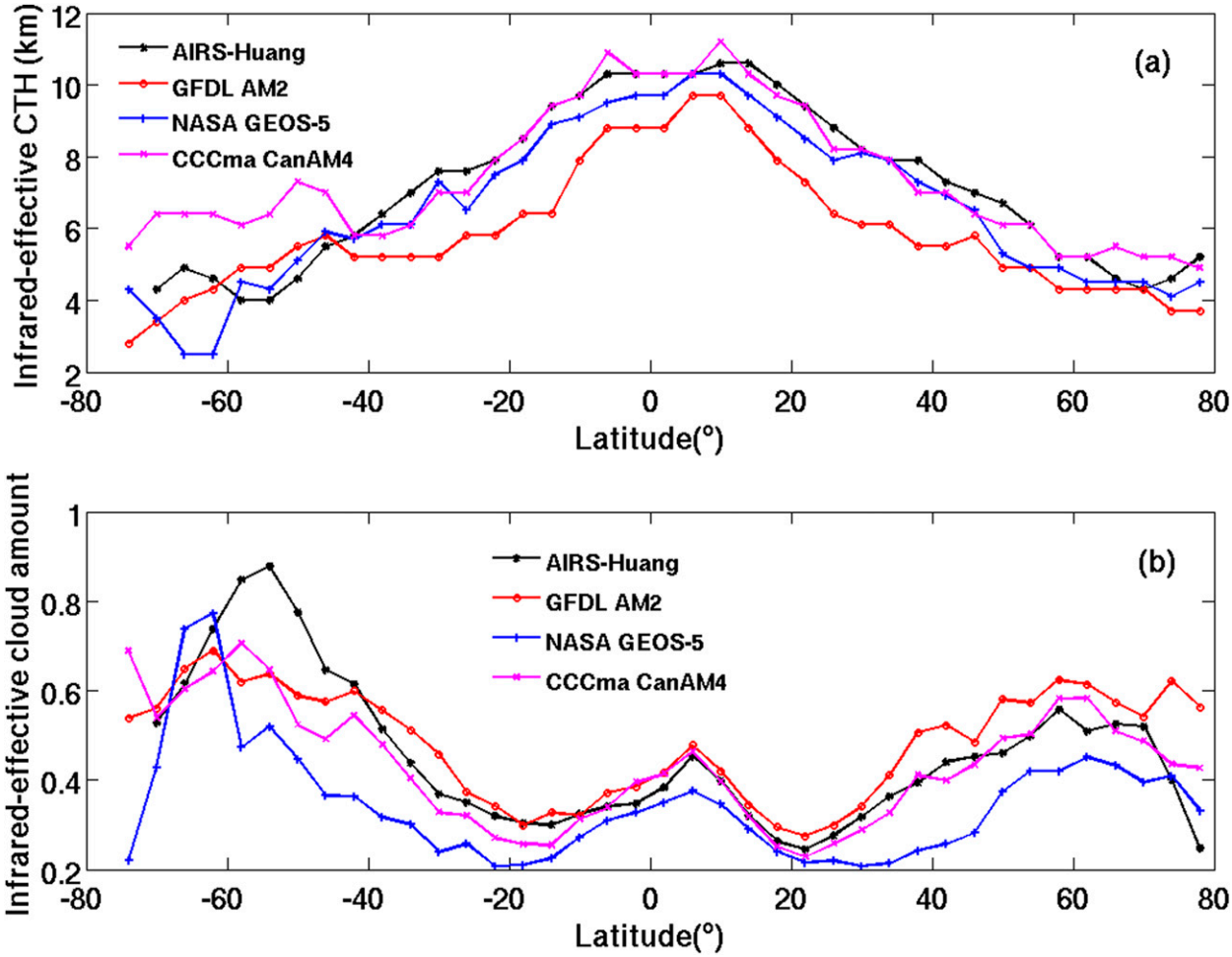

FIG. 9. (a) Zonal-mean IR-effective CTH derived from observed and simulated annual zonal-mean CRE in 2004. All data are shown in 4° latitude intervals. (b) As in (a), but for the IR-effective cloud amount. Black curves are from the inversion of band-by-band CRE from the collocated AIRS and CERES observations. Red, blue, and purple cures are derived from the simulated band-by-band CRE of the GFDL AM2, NASA GEOS-5, and Canadian CCCma CanAM4 GCMs, respectively.

Circulation Model (CanAM4) by the Canadian Centre for Climate Modeling and Analysis (CCCma)]. Relevant details about these GCMs and the methodology for evaluating their band-by-band CREs can be found in Huang et al. (2013) and, for brevity, are not repeated here. In this subsection, we only use these simulations to provide preliminary evidence of the merit of CTH_{eff} and CA_{eff}, instead of a full-scope data–model evaluation. Thus, this section will focus on zonal-mean quantities only.

Figure 9 shows the comparisons of zonal-mean CTH_{eff} and CA_{eff} among these datasets. Global-mean results are listed in Table 2. The overall features of both observations and three GCMs are similar to each other, such as the gradual decrease of CTH_{eff} from the tropics to the poles and the maxima of IR-effective cloud amounts in the ITCZ zone and in the storm-track regions of both hemispheres. However, there are also noticeable differences. CA_{eff}, as inverted from the GEOS-5 band-by-band CREs, is systematically lower by ~10% globally than those from the collocated AIRS and CERES observations and the other two simulations. This underestimation is very likely related to the underestimation of cloud amount by the GEOS-5 model noted previously by other studies (Molod et al. 2012; Sud et al. 2013). In terms of CTH_{eff}, however, the GEOS-5 simulation agrees with observations better than the other two GCMs.

The CanAM4 simulation has higher CTH_{eff} than the observations in both polar regions. This is consistent with the findings in von Salzen et al. (2013), which compared CanAM4 simulations with observations from the *Cloud–Aerosol Lidar and Infrared Pathfinder Satellite Observations* (*CALIPSO*) and found that the simulated cloud tops in both polar regions are higher than observed. Figure 9 and Table 2 clearly show that, although the LW

TABLE 2. The global-mean LW CRE, CTH_{eff}, and CA_{eff} derived from the collocated AIRS and CERES observations in 2004 and from simulations forced by observed SST in 2004 by the GFDL AM2, NASA GEOS-5, and CCCma CanAM4 GCMs.

Global-mean quantities	AIRS and CERES	GFDL AM2	NASA GEOS-5	CCCma CanAM4
LW CRE ($W m^{-2}$)	28.0	26.2	22.8	24.8
CTH_{eff} (km)	7.1	6.4	7.2	7.9
CA_{eff} (%)	42.3	44.9	32.2	40.3

CREs of both GEOS-5 and CanAM4 are considerably lower than those observed, the reasons are different; the discrepancy is largely due to an underestimated global-mean CA_{eff} for the GEOS-5 model and due to an overestimated global-mean CTH_{eff} for the CanAM4 model.

Although the global-mean LW CRE from the GFDL AM2 simulation agrees better with the observed value than that from the other two GCMs, this is achieved by a compensation between CTH_{eff} and CA_{eff}: the GFDL AM2 simulation yields lower CTH_{eff} than its observed counterpart for both the tropics and midlatitudes, but it also has CA_{eff} higher than observed for the same regions. As a result, even though its global mean CTH_{eff} is noticeably lower than the observed one by ~1 km, its LW CRE does not differ from observations as in the GEOS-5 and CanAM4 models. Figure 9 and Table 2 suggest that such discrepancies in CTH and CA can be distinguished via the stepwise inversion of CTH_{eff} and CA_{eff} from the f_{CRE} and LW CRE but not directly from the broadband CRE diagnostics.

5. Conclusions and discussion

We extend the algorithms of Huang et al. (2010) to cloudy-sky observations over the entire globe; hence, spectral flux and spectral cloud radiative effect (CRE) can now be derived from all collocated AIRS–CERES observations. Only scene-type information from the CERES SSF dataset is used in the algorithm, allowing the integral of the derived spectral flux to be independently checked against collocated CERES broadband OLR. The comparison shows that the annual-mean difference between the CERES OLR and the OLR derived from our algorithm is less than 1 $W m^{-2}$ for clear-sky observations and ~(2.0–3.0) $W m^{-2}$ for cloudy-sky observations. The derived OLR also agrees well with CERES OLR in terms of interannual variability. Using multiyear spectral flux and CRE datasets derived from the observations, we depict the climatology of spectral CRE for both the global average and different climate zones. The far-IR contribution to the clear-sky and all-sky OLR, as well as to the LW CRE, is discussed in terms of zonal-mean statistics and the distinct behaviors of the mid-IR and far IR. Although some spectral aspects of the TOA LW radiation budget have been known or can be derived from other venues, this is the first time, to our knowledge, that they are discussed in such detail using satellite observations with global coverage.

We extend the use of spectral CRE and band-by-band CRE in GCM evaluations by defining the IR-effective cloud-top height and IR-effective cloud amount (CTH_{eff} and CA_{eff}). The CTH_{eff} and CA_{eff} derived from monthly-mean band-by-band CRE fields can be related to the CTH and CA from physical cloud retrievals. Although not a one-to-one match by design, both CTH_{eff} and CA_{eff} capture the major spatial and temporal variations of their counterparts from physical retrievals. The concepts of CTH_{eff} and CA_{eff} are less useful in regions with frequent occurrence of optically thin clouds or regions with nearly isothermal atmospheric temperature through the troposphere. The CTH_{eff} and CA_{eff} are directly derived from the LW CRE and f_{CRE}, yet they can be related under many circumstances to the physical cloud fields, allowing them thus to serve as the bridge between diagnostics of TOA radiation budgets and cloud properties affecting the LW radiation. Using three atmospheric GCMs as examples, we demonstrate that the CTH_{eff} and CA_{eff} can help us to properly attribute the discrepancies between modeled and observed LW CRE, something that is not possible with broadband CRE alone. While observed broadband fluxes have been used for decades in model evaluations and have been recently complemented by narrowband radiances from LW radiometers aboard operational weather satellites (e.g., Huang et al. 2005; Turner and Tett 2014), spectral flux and spectral CRE provides another direct and meaningful avenue for model evaluation. Band-by-band flux and CRE are quantities already computed by each model that can reveal discrepancies in the radiation budget, like their broadband counterparts, while pointing toward the inadequacies in temperature, humidity, and cloud simulations that are root causes of the discrepancies, similar to what narrowband radiances can achieve.

A drawback of using satellite data to evaluate GCMs is the inevitable averaging over a wide range of spatial or temporal scales. Given the many nonlinear relations in physical climate systems, averaging satellite data onto monthly periods and coarse GCM grid scales can make the attribution of discrepancies between modeled and observed fields to underlying physical processes a challenging task. Using spectral flux and CRE and their associated products, CTH_{eff} and CA_{eff}, in GCM evaluations can complement the more traditional ways of evaluating models with observed broadband radiation budget and cloud macroscopic properties. The additional spectral dimension provides information about the detailed

nature of the OLR and CRE and their linkage to clouds that cannot be directly obtained from either broadband flux or CRE or cloud retrievals alone.

Both Huang et al. (2013) and this study stress the large discrepancies among three GCMs when their band-by-band CRE is evaluated. It should be expected that other GCMs also have very different band-by-band CRE statistics. One intriguing question to be explored in future studies is to what extent such discrepancies among GCMs with regard to band-by-band CRE can be linked to their discrepancies in longwave cloud feedback strength.

This study also reinforces the finding in Chen et al. (2013) about the importance of the far IR in the TOA radiation budget. It must come to the forefront in remote sensing and radiation budget studies, as there is still much to be observed and understood in terms of the far IR, such as surface spectral emissivity of subpolar land surfaces, the optical properties of cirrus, and the water vapor continuum absorption of this spectral region. Although this series of studies make use of correlations between the mid-IR and far IR to infer the far-IR spectral flux, the ultimate test would still come from direct observations of far-IR spectral radiances from space.

Acknowledgments. We wish to thank Dr. S. Tett and an anonymous reviewer for their thorough and thoughtful comments, which helped us greatly improve the clarity of the presentation. The *Aqua* CERES data were obtained from NASA Langley DAAC and AIRS level 1B data from NASA GSFC DAAC. The ECMWF ERA-Interim data are from http://data-portal.ecmwf.int/data/d/interim_daily/ . The MODIS–CE data were from the Climserv Data Center of IPSL/CNRS. This research is supported by the NASA *Terra/Aqua* program under Grant NNX11AH55G awarded to the University of Michigan. L. Oreopoulos and D.M. Lee also acknowledge support by NASA's Modeling, Analysis, and Prediction Program.

APPENDIX A

Correction Method

The correction method for constructing spectral ADMs for measurements over land is described below. It is based on the spectral ADMs built by Huang et al. (2010) for measurements over ocean.

The core of spectral ADMs is the spectral anisotropic factor x, which connects the spectral flux F and observed spectral radiance R at a given zenith angle θ by

$$F_{1,2} = \frac{\pi R_{1,2}(\mu)}{x_{1,2}}, \tag{A1}$$

where the subscripts 1 and 2 denote ocean and land, respectively, and $\mu = \cos\theta$. For brevity, the subscript υ for the AIRS channel frequency is omitted.

Recall that radiance at the TOA can be written as

$$R_{1,2}(\mu) = \varepsilon_{s_{1,2}} B(T_s) e^{-(\tau/\mu)} + [1 - e^{-(\tau/\mu)}] B(T_e), \tag{A2}$$

where ε_s is the surface spectral emissivity, T_s is the surface temperature, T_e is the one-layer effective temperature of the atmosphere, and τ is the total optical depth of the atmosphere. The spectral flux can be written as

$$F_{1,2} = 2\pi \int_0^1 R_{1,2}(\mu)\mu \, d\mu. \tag{A3}$$

We can write

$$x_2 = x_1(1 + \Delta x), \tag{A4}$$

where Δx is the fractional difference between ocean and land anisotropic factor for the same cloudy subscene type (normally $\Delta x \ll 1$). Note that the atmospheric conditions here are identical, and all differences are caused by ε_{s_1} and ε_{s_2} (i.e., the different surface emissivity). Therefore,

$$\begin{aligned} F_1 - F_2 &= 2\pi \int_0^1 [R_1(\mu) - R_2(\mu)]\mu \, d\mu = 2\pi(\varepsilon_{s_1} - \varepsilon_{s_2}) B(T_s) \int_0^1 e^{-(\tau/\mu)} \mu \, d\mu \\ &= \frac{\pi R_1(\theta)}{x_1} - \frac{\pi R_2(\theta)}{x_1(1 + \Delta x)} \approx \frac{\pi R_1(\theta)}{x_1} - \frac{\pi R_2(\theta)}{x_1}(1 - \Delta x). \end{aligned} \tag{A5}$$

Solving for Δx,

$$\begin{aligned} \Delta x(\theta) &= (\varepsilon_{s_1} - \varepsilon_{s_2}) B(T_s) \left[\frac{2x_1}{R_2(\theta)} \int_0^1 e^{-(\tau/\mu)} \mu \, d\mu - \frac{e^{-(\tau/\mu)}}{R_2(\theta)} \right] \\ &= (\varepsilon_{s_1} - \varepsilon_{s_2}) B(T_s) \left\{ \frac{x_1}{R_2(\theta)} [e^{-\tau} - \tau E_2(\tau)] - \frac{e^{-(\tau/\mu)}}{R_2(\theta)} \right\}, \end{aligned} \tag{A6}$$

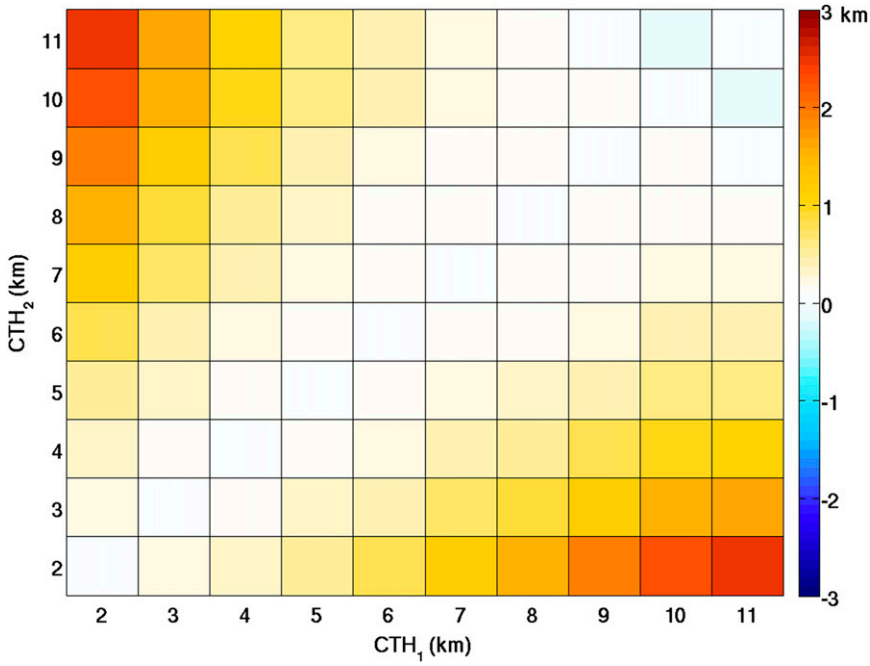

FIG. B1. The difference between CTH_{eff} and monthly-mean physical CTH as a function of cloud-top height. It is assumed that in the first half of month the cloud-top height is CTH_1, while in the second half of month it is CTH_2. The atmospheric profile is assumed to follow the *U.S. Standard Atmosphere, 1976*.

where $E_n(\tau)$ is the nth-order exponent integral function (Goody and Yung 1989). Two asymptotic limits are as follows: when $\tau = 0$ (Lambertian surface and no atmospheric absorption), $\Delta x(\theta) = 0$ (i.e., isotropic radiation); and when $\tau \to +\infty$, $\Delta x(\theta) = 0$ (i.e., opaque atmosphere and surface does not affect TOA radiance at all). It can be easily verified that (A6) is correct for both limits.

Therefore, as long as the value of $\Delta x(\theta)$ is determined, a correction can be made. In the above expression of $\Delta x(\theta)$, ε_{s_1} and ε_{s_2} are known from the ASTER surface spectral emissivity database, x_1 is obtained from the spectral ADMs built in Huang et al. (2010) for the oceans, and $R_2(\theta)$ comes from AIRS radiance observation over the land surface. This leaves optical depth τ being the only unknown variable on the right-hand side. The CERES SSF dataset contains the CERES–MODIS cloud retrievals which assume up to two layers of cloud (Minnis et al. 2011a,b) and retrieve cloud fraction f and cloud optical depth for each layer. We denote the high- and low-level clouds with subscripts h and l, respectively. The effective optical depth τ over the satellite footprint in (A6) can be expressed as

$$e^{-\tau} = f_h e^{-(\tau_h + \tau_{\rm clr})} + f_l e^{-(\tau_l + \tau_{\rm clr})} + (1 - f_h - f_l)\, e^{-\tau_{\rm clr}}, \tag{A7}$$

where $\tau_{\rm clr}$ is the clear-sky optical depth and τ_h, τ_l, f_h, and f_l are all from CERES–MODIS cloud retrievals. For each possible combination of surface temperature and precipitable water for the subscene type definitions (Table 4 in Loeb et al. 2005), we use four months (January, April, July, and October) of ECMWF ERA-Interim 6-hourly profiles to build a lookup table so that $\tau_{\rm clr}$ can be estimated for different seasons and different latitudes. The adoption of this lookup table approach is the reason why we call our correction method semiempirical. By following the above steps, the effective optical depth in (A6) can be derived, and thus the correction of $\Delta x(\theta)$ can be computed.

APPENDIX B

Numerical Simulation to Explain Overestimation

Figure 7 shows that, for regions with large cloud variability, the CTH_{eff} inverted from monthly-mean band-by-band CRE is always higher than the monthly-mean CTH in the MODIS–CE retrievals products. These storm-track regions where cloudiness is dominated by synoptic weather tend to be occupied by different cloud systems in the course of one month. Here we use a simple numerical simulation to explain this overestimation.

We use the *U.S. Standard Atmosphere, 1976* profile and assume that, in the first half of a month, the opaque cloud-top temperature is T_1, and in the second half of the month, it is T_2. The corresponding CTHs are denoted as CTH_1 and CTH_2, respectively. We then compute the monthly-mean band-by-band CRE and use our algorithm to derive the corresponding CTH_{eff}. The true physical CTH averaged over one month would simply be $\overline{CTH} = (CTH_1 + CTH_2)/2$. Then we can plot the difference between CTH_{eff} and $\overline{CTH}$ for arbitrary combinations of CTH_1 and CTH_2 in the troposphere, as shown in Fig. B1. It can be seen that the difference is always positive. The larger the difference between CTH_1 and CTH_2, the larger the difference between CTH_{eff} and $\overline{CTH}$. If the occurrences of two cloud types are not equal, it leads to a change in the magnitude of $CTH_{eff} - \overline{CTH}$ but not the sign. The fundamental reason for this overestimation can be traced to the nonlinear dependence of radiative flux on cloud-top temperature. While the cloud-top temperature is approximately linearly proportional to the cloud-top height, the CRE is not linearly dependent on cloud temperature.

REFERENCES

Anderson, G. P., and Coauthors, 2007: Using the MODTRAN5 radiative transfer algorithm with NASA satellite data: AIRS and SORCE. *Algorithms and Technologies for Multispectral, Hyperspectral, and Ultraspectral Imagery XIII,* S. S. Shen and P. E. Lewis, Eds., International Society for Optical Engineering (SPIE Proceedings, Vol. 6565), 656510, doi:10.1117/12.721184.

Andrews, T., J. M. Gregory, M. J. Webb, and K. E. Taylor, 2012: Forcing, feedbacks and climate sensitivity in CMIP5 coupled atmosphere–ocean climate models. *Geophys. Res. Lett.,* **39,** L09712, doi:10.1029/2012GL051607.

Aumann, H. H., and Coauthors, 2003: AIRS/AMSU/HSB on the Aqua mission: Design, science objectives, data products, and processing systems. *IEEE Trans. Geosci. Remote Sens.,* **41,** 253–264, doi:10.1109/TGRS.2002.808356.

Baldridge, A. M., S. J. Hook, C. I. Grove, and G. Rivera, 2009: The ASTER spectral library version 2.0. *Remote Sens. Environ.,* **113,** 711–715, doi:10.1016/j.rse.2008.11.007.

Bodas-Salcedo, A., and Coauthors, 2011: COSP: Satellite simulation software for model assessment. *Bull. Amer. Meteor. Soc.,* **92,** 1023–1043, doi:10.1175/2011BAMS2856.1.

Cess, R. D., and Coauthors, 1989: Interpretation of cloud-climate feedback as produced by 14 atmospheric general circulation models. *Science,* **245,** 513–516, doi:10.1126/science.245.4917.513.

Chahine, M. T., and Coauthors, 2006: AIRS: Improving weather forecasting and providing new data on greenhouse gases. *Bull. Amer. Meteor. Soc.,* **87,** 911–926, doi:10.1175/BAMS-87-7-911.

Chen, X. H., X. L. Huang, N. G. Loeb, and H. L. Wei, 2013: Comparisons of clear-sky outgoing far-IR flux inferred from satellite observations and computed from the three most recent reanalysis products. *J. Climate,* **26,** 478–494, doi:10.1175/JCLI-D-12-00212.1.

Dee, D. P., and Coauthors, 2011: The ERA-Interim reanalysis: Configuration and performance of the data assimilation system. *Quart. J. Roy. Meteor. Soc.,* **137,** 553–597, doi:10.1002/qj.828.

Garay, M. J., S. P. de Szoeke, and C. M. Moroney, 2008: Comparison of marine stratocumulus cloud top heights in the southeastern pacific retrieved from satellites with coincident ship-based observations. *J. Geophys. Res.,* **113,** D18204, doi:10.1029/2008JD009975.

Goody, R., and Y. Yung, 1989: *Atmospheric Radiation: Theoretical Basis.* Oxford University Press, 519 pp.

Hanel, R. A., B. J. Conrath, V. G. Kunde, C. Prabhaka, I. Revah, V. Salomonson, and G. Wolford, 1972: The Nimbus 4 infrared spectroscopy experiment: 1. Calibrated thermal emission spectra. *J. Geophys. Res.,* **77,** 2629–2641, doi:10.1029/JC077i015p02629.

Harries, J., and Coauthors, 2008: The far-infrared Earth. *Rev. Geophys.,* **46,** RG4004, doi:10.1029/2007RG000233.

Harshvardhan, G. Y. Zhao, L. D. Girolamo, and R. N. Green, 2009: Satellite-observed location of stratocumulus cloud-top heights in the presence of strong inversions. *IEEE Trans. Geosci. Remote Sens.,* **47,** 1421–1428, doi:10.1109/TGRS.2008.2005406.

Huang, X. L., B. J. Soden, and D. L. Jackson, 2005: Interannual co-variability of tropical temperature and humidity: A comparison of model, reanalysis data and satellite observation. *Geophys. Res. Lett.,* **32,** L17808, doi:10.1029/2005GL023375.

——, W. Z. Yang, N. G. Loeb, and V. Ramaswamy, 2008: Spectrally resolved fluxes derived from collocated AIRS and CERES measurements and their application in model evaluation: Clear sky over the tropical oceans. *J. Geophys. Res.,* **113,** D09110, doi:10.1029/2007JD009219.

——, N. G. Loeb, and W. Z. Yang, 2010: Spectrally resolved fluxes derived from collocated AIRS and CERES measurements and their application in model evaluation: 2. Cloudy sky and band-by-band cloud radiative forcing over the tropical oceans. *J. Geophys. Res.,* **115,** D21101, doi:10.1029/2010JD013932.

——, J. N. S. Cole, F. He, G. L. Potter, L. Oreopoulos, D. M. Lee, M. Suarez, and N. G. Loeb, 2013: Longwave band-by-band cloud radiative effect and its application in GCM evaluation. *J. Climate,* **26,** 450–467, doi:10.1175/JCLI-D-12-00112.1.

King, M. D., S. Platnick, W. P. Menzel, S. A. Ackerman, and P. A. Hubanks, 2013: Spatial and temporal distribution of clouds observed by MODIS onboard the Terra and Aqua satellites. *IEEE Trans. Geosci. Remote Sens.,* **51,** 3826–3852, doi:10.1109/TGRS.2012.2227333.

Klein, S. A., and C. Jakob, 1999: Validation and sensitivities of frontal clouds simulated by the ECMWF model. *Mon. Wea. Rev.,* **127,** 2514–2531, doi:10.1175/1520-0493(1999)127<2514:VASOFC>2.0.CO;2.

——, B. J. Soden, and N.-C. Lau, 1999: Remote sea surface temperature variations during ENSO: Evidence for a tropical atmospheric bridge. *J. Climate,* **12,** 917–932, doi:10.1175/1520-0442(1999)012<0917:RSSTVD>2.0.CO;2.

Koelemeijer, R. B. A., P. Stammes, J. W. Hovenier, and J. F. de Haan, 2002: Global distributions of effective cloud fraction and cloud top pressure derived from oxygen A band spectra measured by the Global Ozone Monitoring Experiment: Comparison to ISCCP data. *J. Geophys. Res.,* **107,** 4151, doi:10.1029/2001JD000840.

Kokhanovsky, A., M. Vountas, and J. P. Burrows, 2011: Global distribution of cloud top height as retrieved from SCIAMACHY onboard ENVISAT spaceborne observations. *Remote Sens.,* **3,** 836–844, doi:10.3390/rs3050836.

Loeb, N. G., S. Kato, K. Loukachine, and N. Manalo-Smith, 2005: Angular distribution models for top-of-atmosphere radiative flux estimation from the Clouds and the Earth's Radiant Energy System instrument on the *Terra* satellite. Part I: Methodology. *J. Atmos. Oceanic Technol.,* **22,** 338–351, doi:10.1175/JTECH1712.1.

——, ——, ——, ——, and D. R. Doelling, 2007: Angular distribution models for top-of-atmosphere radiative flux estimation from the Clouds and the Earth's Radiant Energy System instrument on the *Terra* satellite. Part II: Validation. *J. Atmos. Oceanic Technol.,* **24,** 564–584, doi:10.1175/JTECH1983.1.

——, ——, W. Su, T. Wong, F. G. Rose, D. R. Doelling, J. Norris, and X. L. Huang, 2012: Advances in understanding top-of-atmosphere radiation variability from satellite observations. *Surv. Geophys.,* **33,** 359–385, doi:10.1007/s10712-012-9175-1.

McClatchey, R. A., R. W. Fenn, J. E. A. Selby, F. E. Volz, and J. S. Garing, 1972: Optical properties of the atmosphere. 3rd. ed. Air Force Cambridge Research Laboratories Tech. Rep. AFCRL-72-0497, 113 pp. [Available online at http://www.dtic.mil/dtic/tr/fulltext/u2/753075.pdf.]

Menzel, W. P., and Coauthors, 2008: MODIS global cloud-top pressure and amount estimation: Algorithm description and results. *J. Appl. Meteor. Climatol.,* **47,** 1175–1198, doi:10.1175/2007JAMC1705.1.

Minnis, P., and Coauthors, 2011a: CERES edition-2 cloud property retrievals using TRMM VIRS and Terra and Aqua MODIS data—Part I: Algorithms. *IEEE Trans. Geosci. Remote Sens.,* **49,** 4374–4400, doi:10.1109/TGRS.2011.2144601.

——, and Coauthors, 2011b: CERES edition-2 cloud property retrievals using TRMM VIRS and Terra and Aqua MODIS data—Part II: Examples of average results and comparisons with other data. *IEEE Trans. Geosci. Remote Sens.,* **49,** 4401–4430, doi:10.1109/TGRS.2011.2144602.

Molod, A., L. Takacs, M. Suarez, J. Bacmeister, I.-S. Song, and A. Eichmann, 2012: The GEOS-5 Atmospheric General Circulation Model: Mean climate and development from MERRA to Fortuna. NASA Tech. Rep. NASA/TM—2012-104606, 118 pp. [Available online at http://gmao.gsfc.nasa.gov/pubs/tm/docs/Molod484.pdf.]

Pincus, R., S. Platnick, S. A. Ackerman, R. S. Hemler, and R. J. P. Hoffman, 2012: Reconciling simulated and observed views of clouds: MODIS, ISCCP, and the limits of instrument simulators. *J. Climate,* **25,** 4699–4720, doi:10.1175/JCLI-D-11-00267.1.

Rossow, W. B., and R. A. Schiffer, 1991: ISCCP cloud data products. *Bull. Amer. Meteor. Soc.,* **72,** 2–20, doi:10.1175/1520-0477(1991)072<0002:ICDP>2.0.CO;2.

Soden, B. J., I. M. Held, R. Colman, K. M. Shell, J. T. Kiehl, and C. A. Shields, 2008: Quantifying climate feedbacks using radiative kernels. *J. Climate,* **21,** 3504–3520, doi:10.1175/2007JCLI2110.1.

Solomon, S., D. Qin, M. Manning, Z. Chen, M. Marquis, K. Averyt, M. Tignor, and H. L. Miller Jr., Eds., 2007: *Climate Change 2007: The Physical Science Basis.* Cambridge University Press, 996 pp.

Stubenrauch, C. J., and Coauthors, 2013: Assessment of global cloud datasets from satellites: Project and database initiated by the GEWEX Radiation Panel. *Bull. Amer. Meteor. Soc.,* **94,** 1031–1049, doi:10.1175/BAMS-D-12-00117.1.

Sud, Y. C., and Coauthors, 2013: Performance of McRAS-AC in the GEOS-5 AGCM: Aerosol-cloud-microphysics, precipitation, cloud radiative effects, and circulation. *Geosci. Model Dev.,* **6,** 57–79, doi:10.5194/gmd-6-57-2013.

Turner, D. D., and E. J. Mlawer, 2010: The radiative heating in underexplored bands campaigns. *Bull. Amer. Meteor. Soc.,* **91,** 911–923, doi:10.1175/2010BAMS2904.1.

Turner, E. C., and S. F. B. Tett, 2014: Using longwave HIRS radiances to test climate models. *Climate Dyn.,* **43,** 1103–1127, doi:10.1007/s00382-013-1959-6.

von Salzen, K., and Coauthors, 2013: The Canadian Fourth Generation Atmospheric Global Climate Model (CanAM4). Part I: Representation of physical processes. *Atmos.–Ocean,* **51,** 104–125, doi:10.1080/07055900.2012.755610.

Webb, M., C. Senior, S. Bony, and J.-J. Morcrette, 2001: Combining ERBE and ISCCP data to assess clouds in the Hadley Centre, ECMWF and LMD atmospheric climate models. *Climate Dyn.,* **17,** 905–922, doi:10.1007/s003820100157.

Wilber, A. C., D. P. Kratz, and S. K. Gupta, 1999: Surface emissivity maps for use in satellite retrievals of longwave radiation. NASA Tech. Note NASA/TP-1999-209362, 31 pp. [Available online at http://www-cave.larc.nasa.gov/pdfs/Wilber.NASATchNote99.pdf.]